PROCEEDINGS
OF SCIENCE

ONLINE ICRC 2021
THE ASTROPARTICLE PHYSICS CONFERENCE
Berlin | Germany

37ᵗʰ International
Cosmic Ray Conference
12–23 July 2021

Highlights from the GRAPES-3 experiment

P.K. Mohanty,[a,*] **S. Ahmad,**[c] **M. Chakraborty,**[a] **A. Chandra,**[c] **S.R. Dugad,**[a]
U.D. Goswami,[l] **S.K. Gupta,**[a] **B. Hariharan,**[a] **Y. Hayashi,**[b] **P. Jagadeesan,**[a] **A. Jain,**[a]
P. Jain,[d] **S. Kawakami,**[b] **H. Kojima,**[e] **S. Mahapatra,**[i] **P.K. Mohanty,**[a] **R. Moharana,**[j]
Y. Muraki,[g] **P.K. Nayak,**[a] **T. Nonaka,**[h] **A. Oshima,**[e] **B.P. Pant,**[j] **D. Pattanaik,**[a,i]
G.S. Pradhan,[k] **P.S. Rakshe,**[a] **M. Rameez,**[a] **K. Ramesh,**[a] **L.V. Reddy,**[a] **R. Sahoo,**[k]
R. Scaria,[k] **S. Shibata,**[e] **J. Soni,**[d] **K. Tanaka,**[f] **F. Varsi**[d] **and M. Zuberi**[a] **[The
GRAPES-3 Collaboration]**

[a]*Tata Institute of Fundamental Research, Homi Bhabha Road, Mumbai 400005, India*

[b]*Graduate School of Science, Osaka City University, Osaka 558-8585, Japan*

[c]*Aligarh Muslim University, Aligarh 202002, India*

[d]*Indian Institute of Technology Kanpur, Kanpur 208016, India*

[e]*College of Engineering, Chubu University, Kasugai, Aichi 487-8501, Japan*

[f]*Graduate School of Information Sciences, Hiroshima City University, Hiroshima 731-3194, Japan*

[g]*Institute for Space-Earth Environmental Research, Nagoya University, Nagoya 464-8601, Japan*

[h]*Institute for Cosmic Ray Research, Tokyo University, Kashiwa, Chiba 277-8582, Japan*

[i]*Utkal University, Bhubaneshwar 751004, India*

[j]*Indian Institute of Technology Jodhpur, Jodhpur 342037, India*

[k]*Indian Institute of Technology Indore, Indore 453552, India*

[l]*Dibrugarh University, Dibrugarh 786004, India*

E-mail: pkm@tifr.res.in

The GRAPES-3 is a near-equatorial extensive air shower experiment, located in Ooty, India at an altitude of 2200 m above mean sea level. It consists of a dense array of 400 scintillator detectors of 1 m^2 area each with 8 m inter separation. The array triggers showers induced by cosmic ray and gamma ray primaries in the TeV-PeV energy range. An associated muon telescope of 560 m^2 area is designed to record muons above 1 GeV energy in the triggered showers. Additionally, it is designed to trigger on individual muons, providing measurement of muon flux with a statistics of $\sim 4 \times 10^9$ muons per day and an average angular resolution of 4°. In this paper, we summarize the recent results obtained using air shower data on cosmic ray energy spectrum and composition below the Knee, cosmic ray anisotropy, angular resolution, gamma ray source searches and thunderstorm phenomena using the muon flux data.

---

*Presenter

1. Introduction

The origin of cosmic rays (CRs) is a key scientific question in astrophysics since their discovery in 1912 by Victor Hess. Various experimental studies have shown that the cosmic ray spectrum extends over an extra-ordinary energy range (10^8 - 10^{20} eV) and exhibits a power-law behavior. However, the composition and energy spectrum of CRs is not accurately known at $>10^{14}$ eV despite decades of efforts by numerous international groups. Direct experiments have discovered new features in the CR spectrum. For example, a spectral break with a hardening in the spectrum is observed around 300 GeV in proton spectrum by PAMELA [1], AMS-02 [2], DAMPE [3] and CALET [4]. Another spectral break with a softening in the spectrum is observed around 10 TeV in proton spectrum by CREAM [5], DAMPE [3] and CALET [4]. These highlight the importance of precision measurements. However, the direct measurements are limited to energy below 10^{14} eV due to low flux and small area of detectors. The energy range 10^{14}–10^{18} eV which includes the Knee and the Galactic-extragalactic transition region is investigated by the ground-based extensive air shower arrays including KASCADE-Grande [6], GRAPES-3 [7, 8], Tibet AS_γ [9], ARGO-YBJ [10, 11], HAWC [12], IceCube/IceTop [13], Tunka [14]. Several future observatories or upgrade of the existing ones such as LHAASO [15], SWGO [16], TAIGA [17], IceTop [18] will contribute to the Galactic cosmic ray investigations. Giant air shower arrays such as Pierre Auger Observatory and the Telescope array were designed with the primary goal to study ultra-high energy cosmic rays above 10^{18} eV. However, their low energy extensions either under progress or planned would help to study the Galactic-to-extragalactic transition region [19–21]. The GRAPES-3 being the most compact scintillator array among the traditional air shower arrays (scintillator area of GRAPES-3 array is 2% as compared to $< 1\%$ for other arrays) helps in achieving lower energy threshold (90% trigger efficiency at $\sim$50 TeV for protons). The lower threshold energy of the array would allow it to have absolute calibration of cosmic ray energy and composition by comparing results with the direct measurements up to $\sim$100 TeV. The data beyond 100 TeV overlaps with observations by several experiments such as, Tibet, LHAASO, KASCADE, IceTop, HAWC and future observatory such as SWAGO. Moreover, the GRAPES-3 with its largest area muon tracking telescope would provide unique handle on studies of CR composition as well as gamma ray astronomy. Thus, in this scenario, the GRAPES-3 offers certain unique advantages over the other arrays and is expected to contribute significantly to the international efforts foreseen in the next 10 years [22]. In this conference, 13 contributions were made from the GRAPES-3 collaboration [23–35]. However, we discuss of some of the contributions in this paper.

2. The GRAPES-3 experiment

The GRAPES-3 experiment (acronym for **G**amma **R**ay **A**stronomy at **P**eV **E**nergie**S** phase - **3**) is operating at Ooty (11.4°N, 76.7°E, 2200 m altitude) in Tamil Nadu, South India. A schematic of the detectors is shown in Fig.1. The experiment consists of a dense array of 400 plastic scintillator detectors of 1 m^2 each, spread over 25,000 m^2. The scintillator array triggers on showers as low as 1 TeV to well above 10^{16} eV while precisely measuring the shower parameters [8, 36]. It records 3×10^6 showers per day. The median energy of the recorded showers is 15 TeV. The second major component of the experiment is a muon telescope, consisting of 16 modules. Each module has
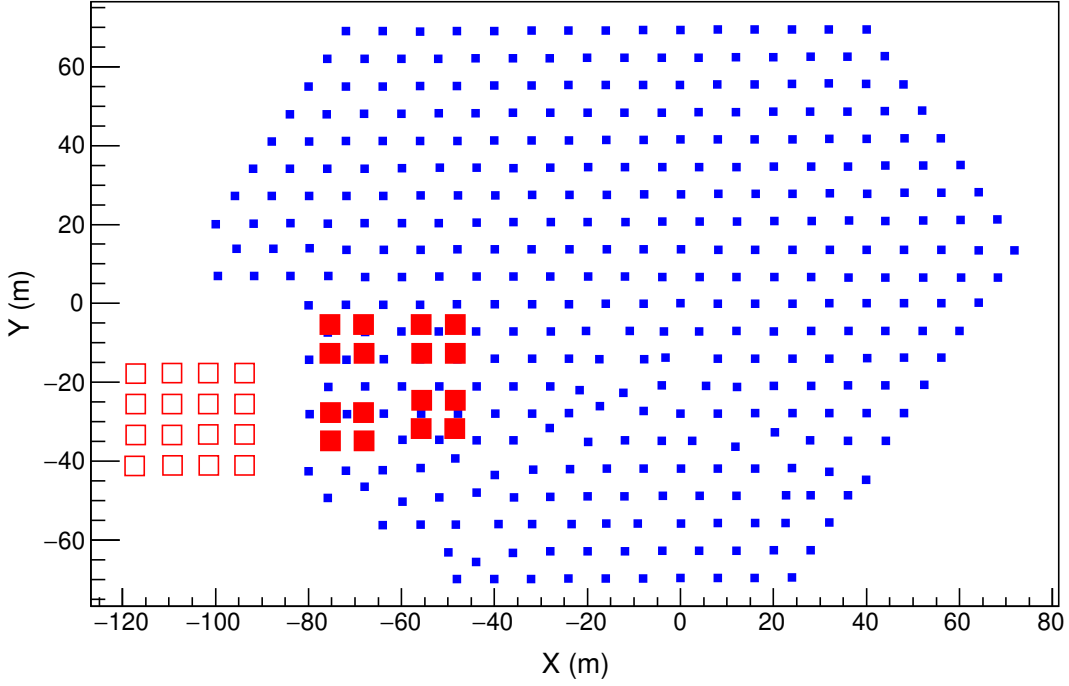
Figure 1: A schematic of the GRAPES-3 array. The blue filled squares represent the existing scintillator detectors of area 1 m² each and the red filled squares represent the existing muon modules of 35 m² area each whereas the open squares represent muon modules under construction.

four layers of proportional counters (PRC) which are made of mild-steel tubes of $0.1 \times 0.1\text{m}^2$ square cross section and 6 m length each. The area of each module is 35 m². Thus, the entire area of the muon telescope is 560 m² area, consisting of total 3712 PRCs [37]. A concrete shielding of 550 g.cm⁻² thickness allows to detect muons above 1 GeV × sec(θ), where θ is the zenith angle. The muons are tracked through four layers of PRCs in each module and the muon contents in each shower is obtained by summing up the muons detected in 16 modules. The muon content is used for measurement of CR composition [7] and rejection cosmic ray background for gamma ray studies. The muon telescope is also designed to trigger on individual muons. About 4×10^9 muons are recorded every day. This data is used to study solar physics, space weather and atmospheric acceleration and has produced exciting results [38, 39]. The scintillator detectors record the density and relative arrival time of secondary particles in each triggered shower which are used to reconstruct the arrival direction of a shower by fitting the shower front [40]. The shower parameters such as core location (X_c, Y_c), size (N_e) and age (s) are obtained by fitting the observed particle densities with Nishimura-Kamata-Greisen (NKG) formula given by Eq.1 through a negative log likelihood minimization algorithm using MINUIT, the details of which can be found elsewhere [7].

$$\rho(r_i) = \frac{N_e}{2\pi r_M^2} \frac{\Gamma(4.5 - s)}{\Gamma(s)\Gamma(4.5 - 2s)} \left(\frac{r_i}{r_M}\right)^{s-2} \left(1 + \frac{r_i}{r_M}\right)^{s-4.5} \tag{1}$$

where r_i is the lateral distance of the ith detector from the shower core, and r_M is the Moliére radius which is 103 m for GRAPES-3.

3. Results

3.1 Cosmic ray energy spectrum and composition

The results on analysis of primary cosmic ray (PCR) energy spectrum and composition over an energy range of 80 TeV to 1.5 PeV were presented at this conference [26]. The data period for this analysis is 1 January 2014 to 31 August 2016. Various stringent criteria were used to select high quality data. These include (1) the shower cores landing well within the array boundary (within 50 m radius from the center of the array), (2) zenith angle is restricted to below $18°$, (3) trigger efficiency greater than 90%, (4) removal of the periods having problems in the trigger or unstable operation of the experiment. The total live time of data collection is 926 days. The number of showers remained after applying all the quality cuts is 3.2×10^7 from a total set of 2.5×10^9 showers.

The mass composition of PCRs was derived using muon multiplicity distribution (MMD) of the observed data by comparing with the MMDs from Monte-Carlo simulations, performed using the CORSIKA package (version 7.69) and QGSJET-II-04 and FLUKA hadronic interaction models for high and low energy, respectively. The simulations were performed for five elements namely H, He, N, Al, and Fe where N, Al and Fe are used to represent (C, N, O), (Mg, Al, Si) (Mn, Fe, Co) masses in PCRs. Fig.2 illustrates the results of a χ^2 minimization of individual simulated MMDs fitting to the MMDs of the observed MMD for a shower size of $10^{4.4}$-$10^{4.6}$. The fraction of the events of each simulated MMD for a given element provides the composition for that element.
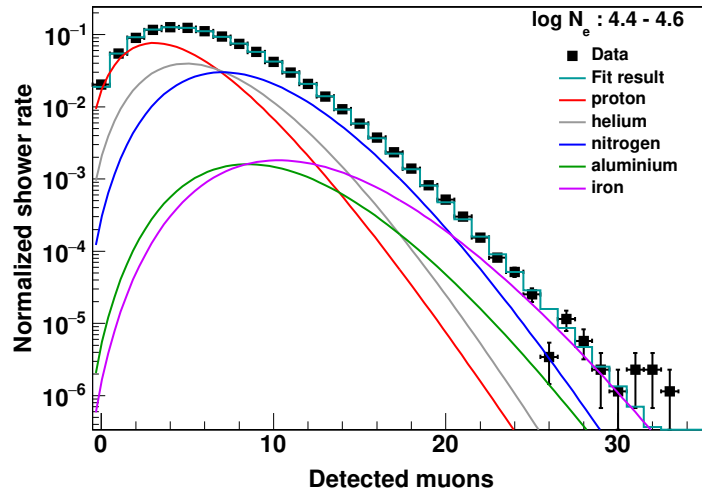
Figure 2: χ^2 minimization of normalized for simulated primaries with observed normalized MMD for 4.4 $\leq \log(N_e) < 4.6$.

The measured preliminary elemental spectrum of proton and helium are plotted along with direct and indirect observations in Fig.3 and Fig.4, respectively. The statistical error bars are smaller than the marker size. The flux of the measured proton spectrum in this work is consistent with CREAM I + III [5] and NUCLEON KLEM [43] (within error) at lower energy and is consistent with KASCADE (QGSJET-01) [45] at higher energy. Similarly, the measured helium spectrum is consistent with CREAM I+III and NUCLEON KLEM (within error) at lower energy.
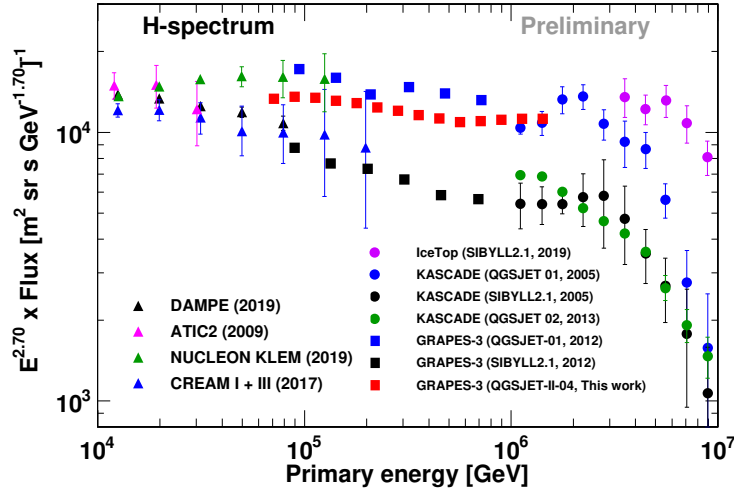
Figure 3: GRAPES-3 proton spectrum results of this work compared with DAMPE [3], ATIC-2 [42], NUCLEON KLEM [43], CREAM [5], GRAPES-3 2012 [7], IceTop [44], KASCADE 2005 [45] and KASCADE 2013 [46].
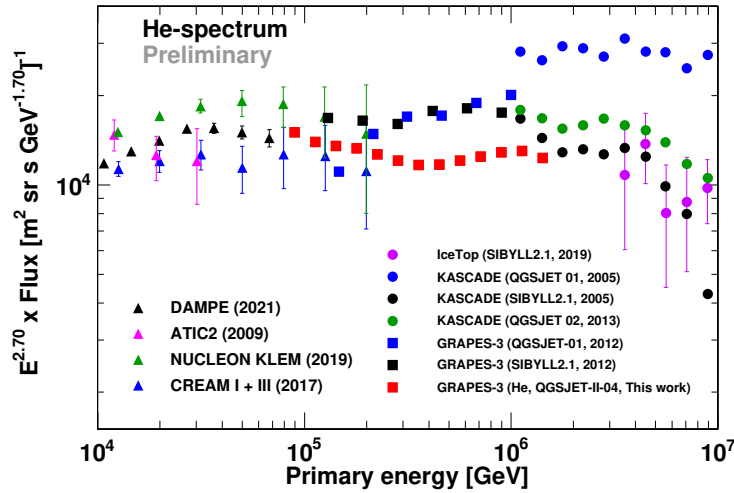
Figure 4: GRAPES-3 helium spectrum results of this work compared with DAMPE [41], ATIC-2 [42], NUCLEON KLEM [43], CREAM [5], GRAPES-3 2012 [7], IceTop [44], KASCADE 2005 [45] and KASCADE 2013 [46].

3.2 Cosmic ray anisotropy

The analysis on cosmic ray anisotropy and preliminary results were presented in the conference [30]. Three years of collected during 1 January 2014 and 31 December 2016 with a total of 3.4×10^9 events were used for this analysis. After applying the various selection criteria, the number of events used for the analysis is 2.49×10^9. The median energy for the event sample is 28.2 TeV. The zenith and azimuth angles were converted to right ascension (α) and declination (δ) and a data map as shown in Fig.5) was generated. To estimate the background, time scrambling method was used

[47, 48]. The relative intensity between the data and scrambled maps provides an estimate of the anisotropy.The anisotropy was calculated by,

$$a = \frac{N_i - N_r}{N_r}$$

where N_i is the number of events in the i-th pixel of the data map and N_r is the number of events in the ith pixel of the weighted scrambled map (Fig. 6). The significance was calculated using the LiMa formula [49]. In this work, the scrambling time window was taken as $\Delta t = 24$ h in solar time. The local arrival distributions and hence the acceptance of the detectors remained stable throughout a period of 24 h.
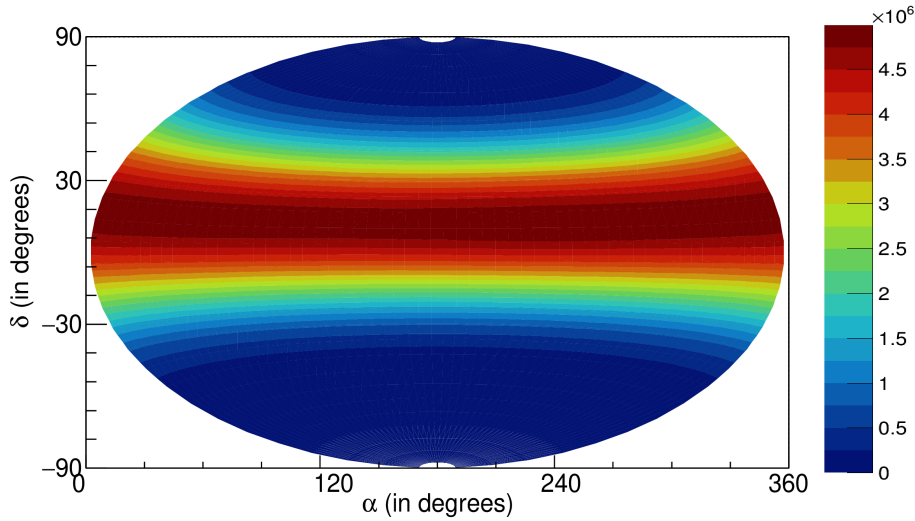
Figure 5: Event distribution in equatorial coordinates. A wide declination range from $-40°$ up to $60°$ is covered

The anisotropy map shown in Fig. 6 exhibits several small scale structures which are consistent with the small-scale anisotropy observed by other experiments. It shows an excess around $45° - 80°$ in right ascension and $-10°$ to $25°$ in declination with an amplitude $\sim 1.2 \times 10^{-3}$ and significance $\sim 2.1\sigma$ (Fig. 7). This region is consistent with the region A structures observed by HAWC [50] and region 1 structures observed by ARGO-YBJ [51]. Another excess region is seen around $110° - 140°$ in right ascension and $-30°$ to $30°$ in declination with a significance $\sim 1.2\sigma$ which has some similarity with the region B structures seen by HAWC and region 2 seen by ARGO-YBJ. A faint deficit structure is also seen with a maximum amplitude of 6×10^{-4} within $200° - 270°$ in right ascension and $-15°$ to $10°$ in declination with a maximum significance $\sim 1.2\sigma$. However, the large scale structures are not observed as they might be getting suppressed due various systematic effects. Further analysis in progress to have a better understanding of various systematics.

3.3 Angular resolution

The GRAPES-3 scintillator detector array was upgraded in late 2012 through installation of in-house developed high performance time-to-digital converters which allowed better measurement
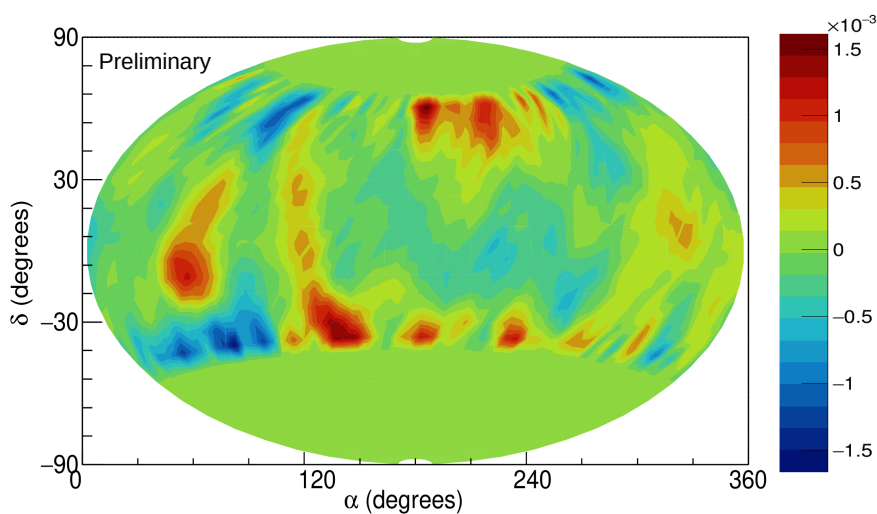
Figure 6: The relative intensity map : Several small scale anisotropic structures are observed.
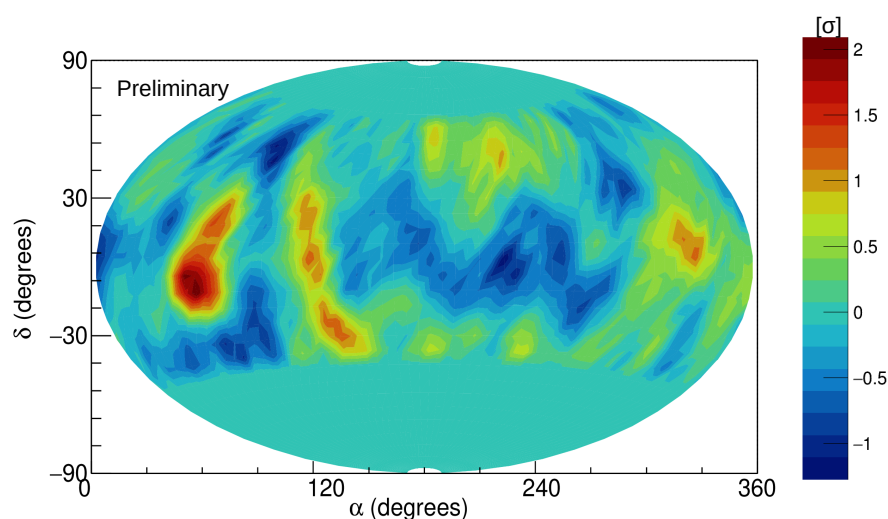
Figure 7: The significance map of the observed anisotropy.

of shower particles arrival time than earlier. The time offsets of the detectors were determined accurately on hourly basis using shower data through a robust technique [40]. The GRAPES-3 angular resolution was measured earlier with the data from the pre-upgrade array and using a fixed curvature for shower front [52]. However, the shower front curvature was studied in detail by exploiting the dependence of shower front curvature on its size and age. After correcting for the curvature, a significant improvement in the angular resolution was achieved as estimated using left-right and even-odd array division methods [40]. In this conference, the angular resolution based on the analysis of the Moon shadow observation was presented [29]. Three years of air shower data (1 January 2014 to 31 December 2016) were analyzed for the Moon shadow observation. In

this analysis, one on-source (real Moon direction) region and a total of six off-source (fake Moon) regions were defined for background calculation, each with $10°$ shifts in azimuth angle successively from the Moon keeping the zenith angle same as the Moon. The observed events were binned in equal incident angle (ψ) bins measured from the center of the Moon.

After subtracting the background, the relative deficit of events were obtained. Results for four different integral energy bins are shown in Fig.8. A clear deficit of events can be seen for each energy bin. The deficit profiles were fitted with a two dimensional Gaussian function to obtain angular resolution. The results are presented in Table 1. The angular resolution as a function of energy is shown in Fig.9. The angular resolution was obtained to be $\sim 1.0°$ above 5 TeV energies with a significance of 11.2σ for the deficit. At energies above 50 TeV, a deficit of 10% has been observed with a significance of 6.6σ and an angular resolution of $\sim 0.54°$. The angular resolution further improves at higher energies as shown in Fig.9.

(a) E > 5 TeV   **(b)** E > 50 TeV

(c) E > 100 TeV   **(d)** E > 250 TeV
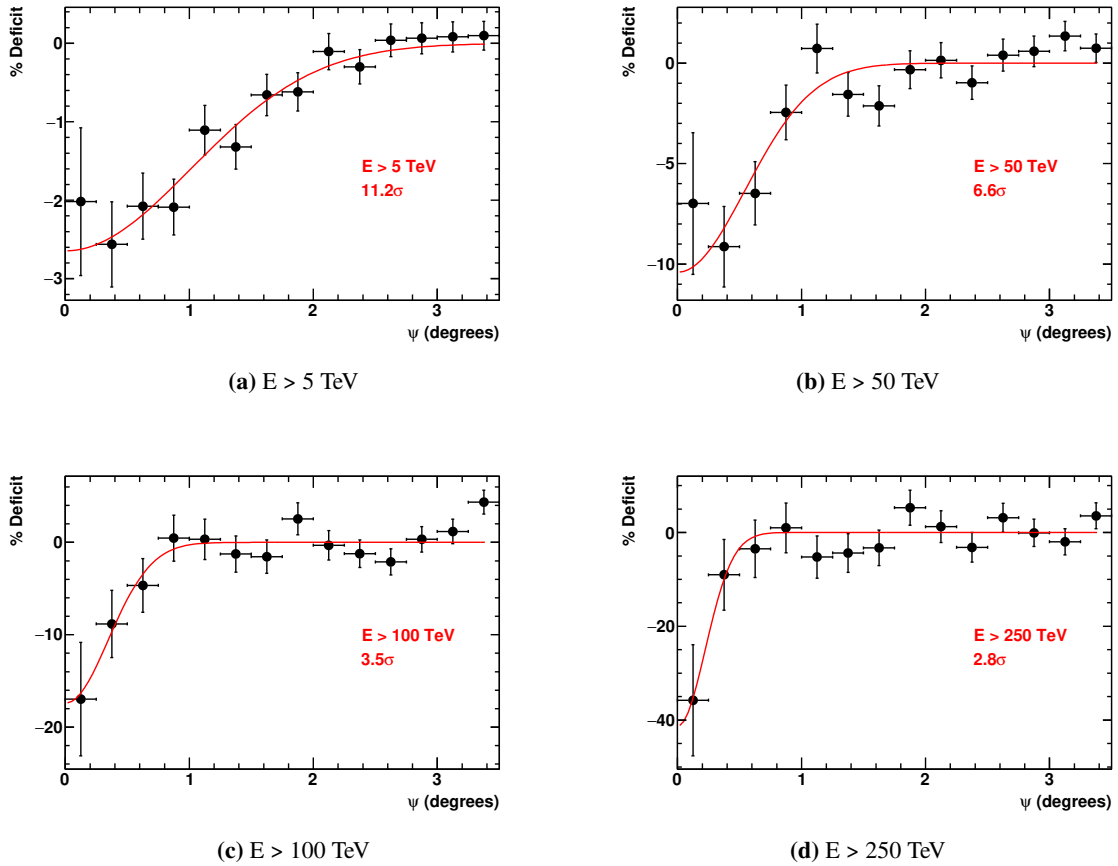
Figure 8: The angular resolutions obtained from the Moon shadow observation are, (a) $1.01° \pm 0.08°$ for E > 5 TeV, (b) $0.54° \pm 0.09°$ for E > 50 TeV, (c) $0.35° \pm 0.08°$ for 100 TeV and (d) $0.23° \pm 0.08°$ for E > 250 TeV with a significance of 11.2σ, 6.6σ, 3.5σ and 2.8σ respectively. The deficit profiles were fitted with a two dimensional Gaussian function as represented by red lines to obtain angular resolution.

Table 1: Results obtained from the Moon shadow observation.

Energy (TeV)	Angular resolution (°)	Maximum deficit (%)	Significance
> 5	1.01 ± 0.08	2.5 ± 0.5	11.2σ
> 50	0.54 ± 0.09	10 ± 2.0	6.6σ
> 100	0.35 ± 0.08	19 ± 6.1	3.5σ
> 250	0.23 ± 0.08	40 ± 12	2.8σ
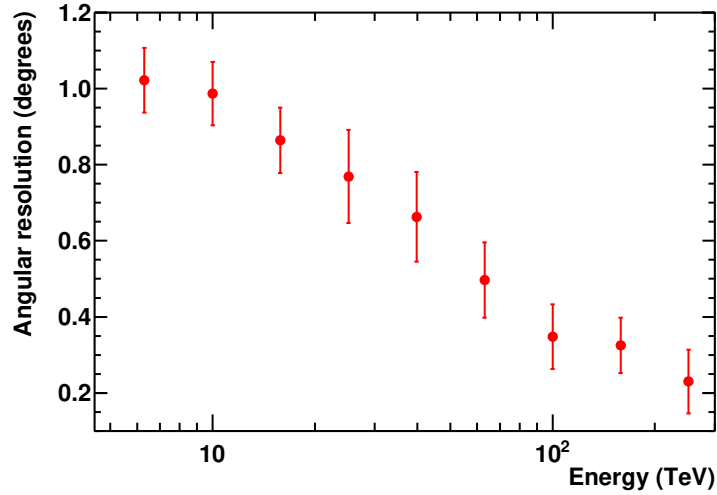
Figure 9: GRAPES-3 angular resolution obtained from the observation of Moon shadow as a function of integral energy.

3.4 Gamma ray search from Crab nebula

To enable detection of gamma rays, high rejection of cosmic ray background is necessary. Cosmic rays produce higher number of muons in air shower than gamma rays. The GRAPES-3 experiment records the muon content in each air shower through muon telescope 16 modules. The air showers with zero muons ($N_{\mu=0}$) are considered to be gamma like showers, while the rest are treated as cosmic rays ($N_{\mu\geq1}$). Cosmic ray rejection efficiency based zero muon criteria was obtained. The rejection efficiency as a function of distance from the shower core is shown in Fig.10. The rejection efficiency decreases with increasing core distance which can be explained by the fact that cosmic ray showers appears to be gamma like showers at larger distances. Fig.11 shows the average rejection efficiency (integrated over all distances) as a function of energy. For the showers above 50 TeV Energy, the rejection efficiency is ~97%, while for showers above 100 TeV Energy, the rejection efficiency is >99.7%.

In order to understand the effectiveness of the background rejection based on the muon content, the background level for 8 off-source regions was studied by shifting the Crab Nebula position by $10°$ in azimuth, while keeping the zenith angle same. The average background was obtained and the results are shown in Fig.12. For energy E > 50 TeV, the background events were reduced by ~97% and ~99.7% for energy E > 100 TeV. The event distribution from the on source region of the
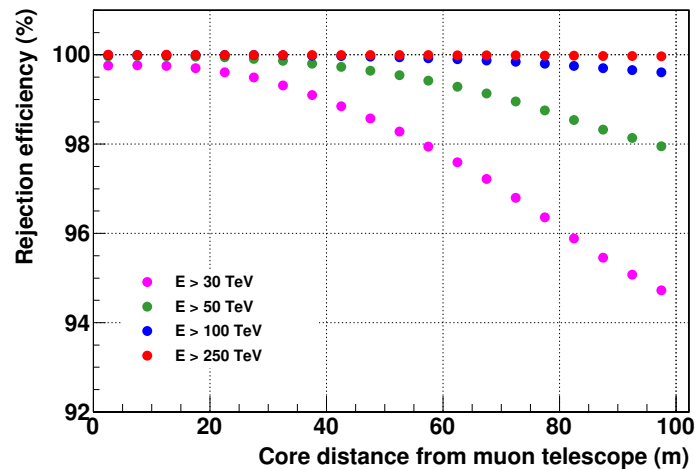
Figure 10: Cosmic ray rejection efficiency as a function of shower core distance from the center of the muon telescope at different energies.
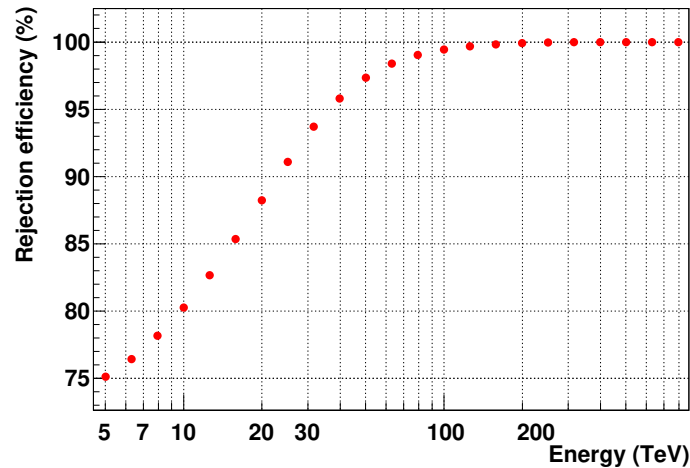
Figure 11: Cosmic ray rejection efficiency as a function of energy

Crab was studied by rejecting cosmic ray events based on muon content. The results are shown in Fig.13 along with the background level represented by dashed lines. From the preliminary studies, no significant excess in the gamma ray events was observed from the direction of the Crab Nebula. However, studies are in progress to understand the various systematics.

3.5 Isotropic diffuse gamma ray flux

The results of the isotropic diffuse gamma ray analysis using one year of shower data recorded between January 01 to December 31, 2014 were presented in this conference [34]. A detailed Monte-Carlo simulation of the air shower development with primary gamma rays using the CORSIKA v7.4001 code was performed to obtain the muon number distribution and estimate the median gamma-ray energy. The hadronic interaction models used are SIBYLL 2.1 and FLUKA 2011, for

(a) Energy > 50 TeV
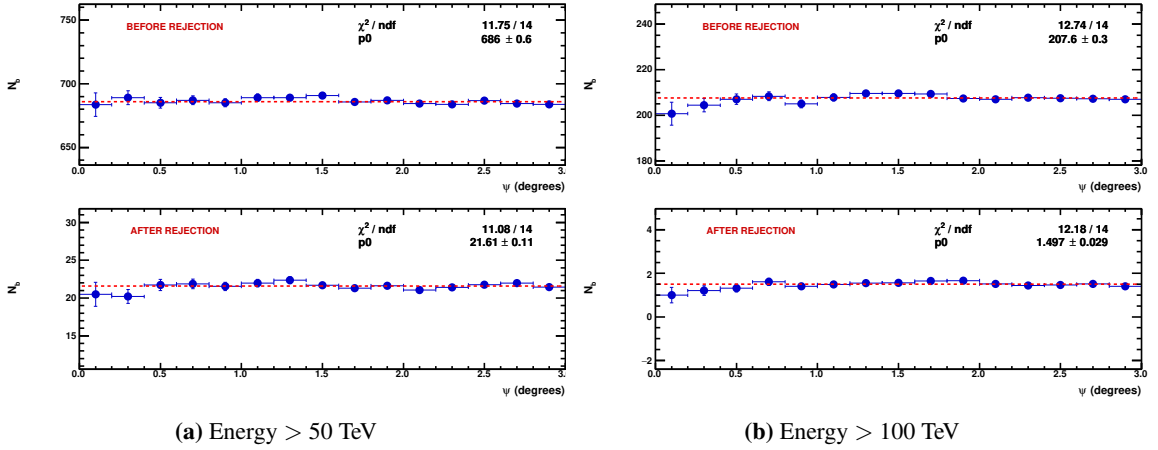
(b) Energy > 100 TeV

Figure 12: Observed background level as a function of incident angle (ψ) measured from the direction of off-source, before and after the rejection of the cosmic rays based on the muon content. For (a) Energy > 50 TeV, $\sim 97\%$ and (b) for energy > 100 TeV, $\sim99.7\%$ of the background cosmic rays are rejected.

(a) Energy > 50 TeV

(b) Energy > 100 TeV
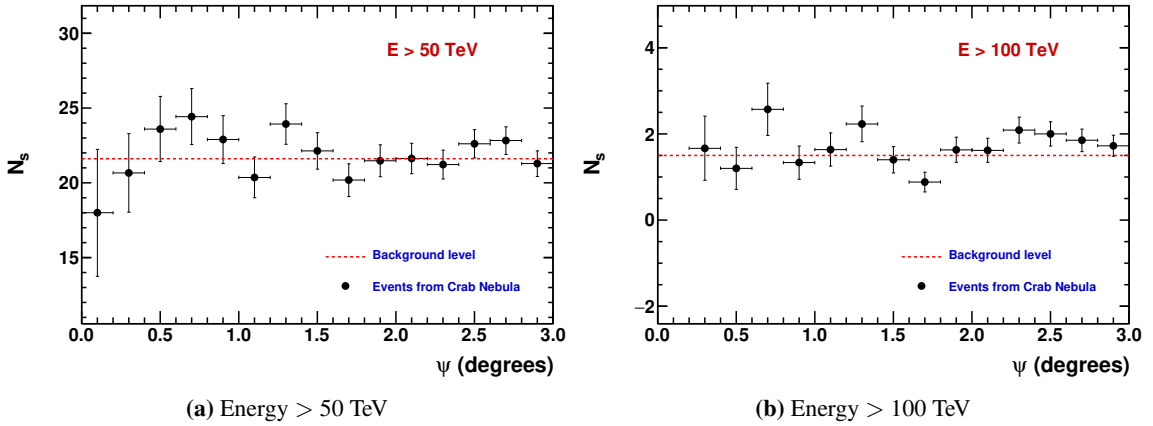
Figure 13: Observed events from the direction of the Crab Nebula plotted with the average background level as a function of incident angle (ψ).

high and low energy, respectively. The showers are generated in the energy range 5 TeV to 10 PeV and zenith angle 0–60° with a differential energy spectrum of $E^{-2.7}$.

The selection efficiency, ϵ_γ, from the gamma ray simulation by taking the ratio of muon poor showers to the total number of incident gamma showers for each radial bin of 5 m from the center of the muon telescope and logarithmic size bin of 0.2 was obtained. Similarly, the cosmic ray rejection efficiency from the one year data by taking the ratio of showers with at least one or more muons to the total incident showers for each radial and logarithmic size bin as before was calculated. A radial distance of up to 30 m from the center of the muon telescope was used for this analysis. In Figure 14, variation of gamma-ray selection and cosmic ray rejection efficiency with energy is plotted for the selected radial distance.

(a) Energy > 50 TeV

(b) Energy > 100 TeV
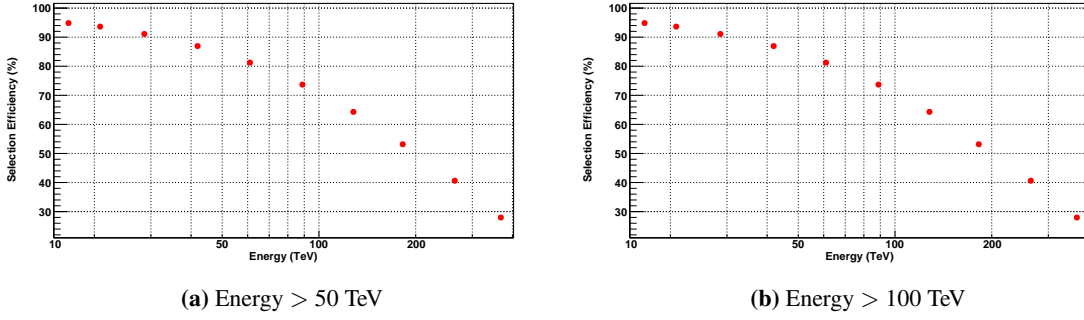
Figure 14: Gamma-ray selection (top) and cosmic-ray rejection efficiency (bottom) as a function of energy for radial distance of 30 m from the muon telescope center

The upper limit on the ratio of gamma-ray over cosmic ray integral flux is determined by [58]:

$$\frac{I_\gamma}{I_{CR}} \leq \frac{N_{90\% \, C.L.}^{\mu=0}}{N_{tot}} \frac{1}{\epsilon_\gamma} \frac{1}{1 - n_{chance}} \tag{2}$$

where $N_{90\% \, C.L.}^{\mu=0}$ is the 90% confidence limit on the number of muon-poor showers assuming Poisson distribution, N_{tot} is the total number of showers, ϵ_γ is the selection efficiency and n_{chance} is the average number of muons due to chance coincidence.

The upper limit results with 90% C.L. on the fraction of gamma ray to cosmic ray flux at energies between 10–300 TeV were determined and the results are shown in 15 along with the results from other experiments. The best upper limits are obtained: $I_\gamma/I_{CR} < 6.18 \times 10^{-5}$ for 182 TeV and $I_\gamma/I_{CR} < 4.51 \times 10^{-5}$ for 265 TeV.

3.6 Thunderstorm acceleration

The GRAPES-3 experiment reported the measurement of 1.3 GV potential in one of the massive thunderclouds recorded on 1 December 2014 by making use of the muon imaging technique [38]. This measurement is ten times larger than the maximum potential reported previously by balloon and rocket sounding measurements. The measurements rely on the precise estimate of the change in the angular muon flux caused by the acceleration of muons during their passage through the charged layers of thunderstorms. The electric potential is estimated with the help of Monte Carlo simulations by using CORSIKA and other in-house tools. A detailed summary on the angular distribution of 487 thunderstorm events recorded during April 2011 to December 2020 was presented during this conference [24]. Though the GRAPES-3 muon telescope is being operated more than two decades, the electric field measurements required to study the thunderstorm effects are actually available since April 2011 with the installation of electric field mills around GRAPES-3. The angular distribution of the events in the 9 directions of the muon telescope is shown in Table.2. About 80% events are observed to be from the East direction. As explained in [38], the variation in the muon intensity (decrease or increase depending the electric field polarity in the cloud) during thunderstorm is observed since the muon charge ratio ($\mu_R = \mu^+/\mu^-$) is greater than one. To understand the asymmetry, investigations were carried out based on CORSIKA simulations. The obtained μ_R from the simulations is shown in Fig.16. It can be clearly seen that the μ_R is close
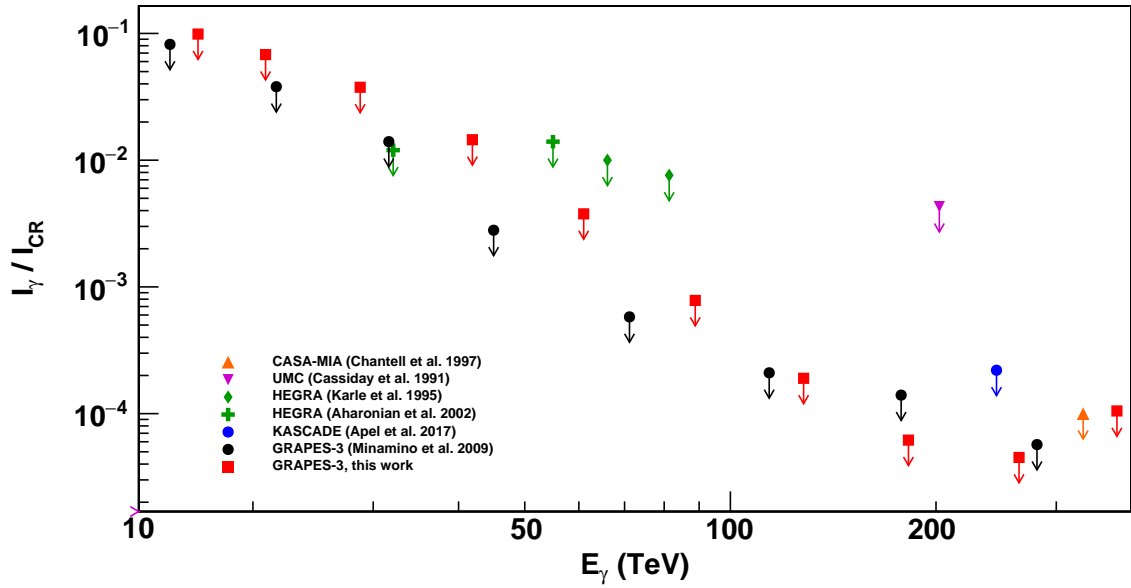
Figure 15: Upper limit measurements of the fraction of isotropic gamma-rays relative to cosmic rays. The points with arrows represent 90% C.L. upper limits from the CASA-MIA [53], UMC [54], HEGRA [55, 56], KASCADE [57], GRAPES-3 [58] and this work, as indicated in the legend.
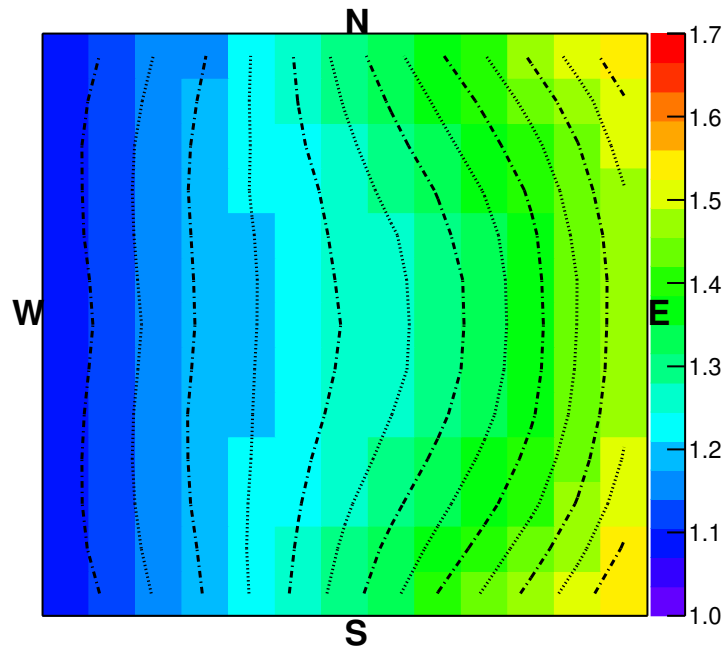
Figure 16: Distribution of μ_R for GRAPES-3 FOV in 169-direction configuration.

to one in west direction whereas it is largest in the east direction. The earth's magnetic field plays a crucial role in bending of particle trajectories outside and inside the atmosphere for primary and secondary particles respectively. The distribution of magnetic field produces an asymmetry in μ_R which may explain the asymmetry in thunderstorm event distribution.

13

NW		N		NE
	6.2%	1.8%	30.1%	
W	0.6%	0.2%	2.8%	E
	7.0%	2.8%	48.6%	
SW		S		SE

Table 2: Thunderstorm event distribution in GRAPES-3 field of view recorded during 2011-2020. Events in the vertical direction is at the center of the table.

4. Summary and future outlook

During the conference, several results were presented from the GRAPES-3 experiment including on cosmic ray energy spectrum and composition, cosmic ray anisotropy, angular resolution, search for gamma ray sources etc. The energy spectrum results on proton and helium show that GRAPES-3 measurements could provide a bridge between direct and indirect measurements. The high angular resolution achieved recently which is verified by the observation of Moon shadow together with high rejection of cosmic ray background based on the muon content enrich the GRAPES-3 potential for multi-TeV gamma ray studies. High statistics and directional muon flux measurement is a unique capability of the GRAPES-3 muon telescope for study of atmospheric and solar phenomena. The upgrade of the muon telescope is in progress to double the area which will enhance the physics potentials of the GRAPES-3 experiment.

References

[1] O. Adriani et al., Science **332** (2011) 69.

[2] M. Aguilar et al., Phys. Rev. Lett. **114** (2015) 171103.

[3] DAMPE Collaboration, Q. An et al., Science Advances **5, 9** (2019) eaax3793.

[4] O. Adriani et al., Phys. Rev. Lett. **122** 181102.

[5] Y. S. Yoon et al., Astrophys. J. 839:5 (2017).

[6] KASCADE-Grande Collaboration, W. D. Apel et al., Phys. Rev. Lett. **107** (2011) 171104.

[7] H. Tanaka et al., J. of Phys. G: Nucl. Part. **39** (2012) 025201.

[8] F. Varsi et al., PoS (ICRC2019) **358** (2019) 449.

[9] M. Amenomori et al., Advances in Space Research **47** (2011) 629.

[10] B. Bartoli et al., Phys. Rev. D **91**(2015) 112017.

[11] B. Bartoli et al., Phys. Recv. D **92** (2015) 092005.

[12] HAWC Collaboration, R. Alfaro et al., Phys. Rev. D **96** (2017) 122001.

[13] M.G. Aartsen et al., Phys. Rev. D **100** (2019) 082002.

[14] N.M. Budnev et al., Astropart. Phys. **117** (2020) 102406.

[15] H. He for the LHAASO Collaboration, Radiat. Detect. Technol. Methods **2** (2018) 7.

[16] H. Schoorlemmer for SWGO collaboration, PoS (ICRC2019) 785.

[17] TAIGA Collaboration, N. Budnev et al., JINST **9** (2014) C09021.

[18] A. Haungs for the IceCube Collaboration, EPJ Web of Conferences **210** (2019) 06009.

[19] S. Ogio for the Telescope Array Collaboration, JPS Conf. Proc. **19** (2018) 011026.

[20] D. Bergman et al., PoS ICRC2017 (2018) 415.

[21] Pierre Auger Collaboration, arXiv:1604.03637 [astro-ph.IM].

[22] A. Haungs et al., Snowmass2021 - Letter of Interest.

[23] A. Jain et al., PoS(ICRC2021) **395** (2021) 257.

[24] B. Hariharan et al., PoS(ICRC2021) **395** (2021) 378.

[25] B. Hariharan et al., PoS(ICRC2021) **395** (2021) 379.

[26] F. Varsi et al., PoS(ICRC2021) **395** (2021) 388.

[27] M. Zuberi et al., PoS(ICRC2021) **395** (2021) 389.

[28] M. Zuberi et al., PoS(ICRC2021) **395** (2021) 390.

[29] D. Pattanaik et al., PoS(ICRC2021) **395** (2021) 391.

[30] M. Chakraborty et al., PoS(ICRC2021) **395** (2021) 393.

[31] M. Chakraborty et al., PoS(ICRC2021) **395** (2021) 394.

[32] A. Chandra et al., PoS(ICRC2021) **395** (2021) 396.

[33] D. Pattanaik et al., PoS(ICRC2021) **395** (2021) 870.

[34] B.P. Pant et al., PoS(ICRC2021) **395** (2021) 871.

[35] H. Kojima et al., PoS(ICRC2021) **395** (2021) 1303.

[36] B. Hariharan et al., Experimental Astronomy **50** (2020) 185.

[37] Y. Hayashi et al., Nucl. Instr. Meth. A **545** (2005) 643.

[38] B. Hariharan et al., Phys. Rev. Lett. **122** (2019)105101.

[39] P.K. Mohanty et al., Phys. Rev. Lett. **117** (2016) 171101.

[40] V.B. Jhansi et al., J. Cosmol. Astropart. Phys. **07** (2020) 024.

[41] F. Alemanno et al., Phys. Rev. Lett. **126** (2021) 201102.

[42] Panov et al., Bulletin of the Russian Academy of Sciences: Physics **73** (2009) 564.

[43] E. V. Atkin et al., Astronomy Reports **63** (2019) 1.

[44] M.G. Aartsen et al., Phys. Rev. D **100** (2019) 082002.

[45] T. Antoni et al., Astropart. Phys. **24** (2005) 1.

[46] W.D. Apel et al., Astropart. Phys. 47 (2013) 54.

[47] Alexandreas et al., Nucl. Instr. Meth. Phys. Res. A **328** (1993) 570.

[48] M. G. Aartsen et al., Astrophys. J. **826** (2016) 220.

[49] T. Li and Y. Ma, Astrophys. J. **272** (1993) 317.

[50] A. U. Abeysekara et al., Astrophys. J. **796** (2014) 108.

[51] B. Bartoli et al., Phys. Rev. D **88** (2013) 082001.

[52] A. Oshima et al., Astropart. Phys **33** (2010) 97.

[53] M.C. Chantell et al., Phys. Rev. Lett. **79** (1997) 1805.

[54] J. Matthews et al., Astrophys. J. **375** (1991) 202.

[55] A. Karle et al., Phys. Lett. B **347** (1995) 161.

[56] F.A. Aharonian et al., Astropart. Phys. **17** (2002) 459.

[57] W. D. Apel, Astrophys. J. **848** (2017) 1.

[58] M. Minamino et al., Proc. of the 31st ICRC (Lodz) (2009).